

# An Adaptive Filter Based Motion Artifact Cancellation Technique Using Multi-Wavelength PPG for Accurate HR Estimation

Pangi Park<sup>✉</sup>, Graduate Student Member, IEEE, Woobean Lee<sup>✉</sup>, Student Member, IEEE, and SeongHwan Cho<sup>✉</sup>, Senior Member, IEEE

**Abstract**—This article presents a motion artifact (MA) cancellation technique for accurate photoplethysmography (PPG)-based heart rate (HR) estimation. The MA is canceled using two PPG signals, measured with closely placed red and green LEDs. The proposed technique utilizes the characteristics of the two PPG signals: the high correlation in MA and their different AC/DC ratios. These characteristics allow the MA to be canceled by an adaptive filter while preserving the AC components. In addition, the use of the sign-sign least mean square (SS-LMS) algorithm for the adaptive filter minimizes the hardware resource requirements. To validate the technique, a prototype was implemented and experiments were conducted with six subjects performing three types of movements: walking, running, and squatting. The proposed MA cancellation method significantly reduced the mean absolute error (MAE) in HR estimation, from 9.83 bpm to 1.48 bpm on average, compared to the conventional bandpass filtered green PPG.

**Index Terms**—Adaptive filtering (AF), ambient light cancellation (ALC), correlated double sampling (CDS), heart rate (HR) estimation, motion artifact cancellation (MAC), photoplethysmography (PPG), sign-sign least mean squares (SS-LMS) algorithm.

## I. INTRODUCTION

WEARABLE devices for daily monitoring of vital signs have received much interest in the recent decade as they can provide an important baseline for health assessment. Among the vital signs, continuous monitoring of heart rate (HR) is particularly valuable for the early detection of various cardiovascular diseases (CVD) [1]. For HR monitoring, electrocardiography (ECG) and photoplethysmography (PPG) based HR monitors are widely used, since both can provide

Manuscript received 9 April 2023; revised 4 June 2023 and 25 July 2023; accepted 23 August 2023. Date of publication 14 September 2023; date of current version 29 November 2023. This work was supported in part by the Institute of Information & Communications Technology Planning & Evaluation (IITP) funded by the Korea Government, MSIT, under Grant 2019-0-00826, High resolution intelligent Radcomm system, and in part by the National R&D Program through the National Research Foundation of Korea (NRF) funded by Ministry of Science and ICT under Grant 2020M3H2A107804514. This paper was recommended by Associate Editor Y. Li. (*Corresponding author: SeongHwan Cho*)

The authors are with the School of Electrical Engineering, Korea Advanced Institute of Science and Technology, Daejeon 34141, Republic of Korea (e-mail: pangipark@kaist.ac.kr; vvalex1@kaist.ac.kr; chosta@kaist.ac.kr).

Color versions of one or more figures in this article are available at <https://doi.org/10.1109/TBCAS.2023.3315297>.

Digital Object Identifier 10.1109/TBCAS.2023.3315297

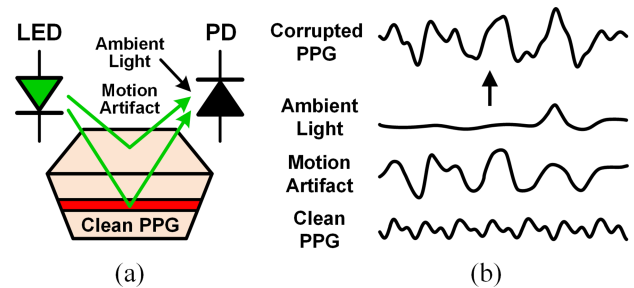


Fig. 1. (a) Typical reflective-mode PPG signal acquisition including artifacts such as ambient light and motion artifacts. (b) Example of a corrupted PPG signal with its components.

non-invasive and wearable solutions. Although ECG-based HR monitors have been widely used due to their high accuracy, they can be uncomfortable as multiple electrodes must be attached to the body. By contrast, PPG-based HR monitoring does not require any electrodes, and the signal can be obtained from a single measurement spot such as a finger or wrist. Therefore, PPG-based HR monitors are included in many of the recent commercial devices such as fitness smartwatches despite their limited accuracy compared to the ECG counterpart [1], [2], [3], [4].

The accuracy limitation of PPG-based heart rate monitors arises because the PPG signal can be easily corrupted by artifacts. A typical situation of PPG signal acquisition, where artifacts such as ambient light and motion artifacts (MA) are present, is illustrated in Fig. 1(a). A clean PPG signal without any artifacts consists of a large non-pulsatile DC component and a small pulsatile AC component that contains the HR information [5], [6]. However, the small pulsatile component is easily buried by the artifacts as shown in Fig. 1(b). Moreover, the artifacts cannot be simply removed by a bandpass filter, since the artifacts typically lie in the same frequency band as the signal of interest.

To suppress the artifacts, various cancellation techniques have been explored. For ambient light, correlated double sampling (CDS) is a common solution. This method requires only an additional sample taken with the LED turned off, which is then subtracted from the subsequent PPG sample. This process is straightforward to implement within a single chip, leading to the wide inclusion of CDS in recently presented PPG readouts [7].

For motion artifacts, several approaches have been proposed. One approach is to use a motion sensor, typically a 3-axis accelerometer, to cancel the motion artifact based on the motion sensor output [8], [9], [10], [11]. However, this method may have limited efficacy because the accelerometer often fails to represent the MA in the PPG accurately, given that motion manifests itself differently to the PPG and the motion sensor [12], [13]. An additional drawback is that the required accelerometer increases hardware complexity.

MA cancellation techniques that do not rely on a motion sensor have been proposed in [14], [15]. In [14], a noise reference signal representing MA is synthesized from the corrupted PPG signal itself, and the MA component in the PPG is canceled based on this synthesized signal. Techniques such as Fast Fourier transform (FFT), singular value decomposition (SVD), and independent component analysis (ICA) are used for the synthesis of the noise reference signal. In [15], a Fourier decomposition method (FDM) is used to decompose the PPG signal into several components. A clean PPG signal is then obtained by superimposing the components that constitute the PPG signal. However, decomposition algorithms are not very effective when the frequency of the motion artifact overlaps with the HR frequency. In addition, the real-time operation of ICA, SVD, and FDM requires an expensive processing unit, which increases the cost and power of the system.

In recent years, MA cancellation techniques using multi-wavelength PPG have been proposed [13], [16], [17]. In [16], an adaptive filter based MA cancellation method is proposed using red and IR PPGs. To remove the tissue effect, which is the main source of error in HR estimation, the red and IR signals are subtracted from each other, under the assumption that the tissue effect is wavelength-independent. The red PPG signal is further enhanced by normalized least mean square (NLMS) algorithm with the subtracted signal. In [13], an IR PPG is used as a motion sensor to cancel the MA in a green PPG, as IR PPG has a high MA-to-signal ratio. After applying continuous wavelet transform (CWT) to both PPG signals, their spectra are normalized and subtracted to cancel MA components. In [17], 12-channel PPG signals are used for motion artifact cancellation. The measurement device consists of four perpendicularly placed PPG modules, each equipped with green, red, and IR LEDs. This configuration allows the sensor to capture the three-dimensional spatial effects of motion. Signal processing methods such as ICA and truncated-SVD are applied to extract the principal component corresponding to the PPG signal. These approaches described above utilize the different characteristics of PPG signals measured using different wavelengths of light. However, MA cancellation using these approaches also requires expensive processing units to implement sophisticated signal processing techniques which is not desirable in resource-constrained wearable devices.

In this article, we propose an adaptive filter based motion artifact cancellation technique using multi-wavelength PPG signals, which does not require an external motion sensor and a heavy processing unit [18]. For MA cancellation, we leverage two key properties of red and green PPG signals measured by closely placed LEDs: highly correlated MA components and different

AC/DC ratios. By applying these PPG signals as inputs to the adaptive filter, the MA can be effectively canceled without a motion reference signal from a motion sensor. Additionally, the use of the sign-sign least mean square (SS-LMS) algorithm for the adaptive filter minimizes hardware resource requirements. To validate our technique, we implemented a prototype and conducted experiments with six subjects performing various activities, such as squatting, walking, and running. Using our proposed technique, the mean absolute error (MAE) in HR estimation was significantly reduced from 9.83 bpm to 1.48 bpm compared to the bandpass filtered PPG signal, corresponding to an 85.0 % reduction in error.

The remainder of the article is organized as follows. In Section II, the PPG signal model including the MA is described. Next, the principle of the proposed MA cancellation technique is presented in Section III. The system architecture and the detailed implementation of the prototype are described in Section IV, and the measurement results of the prototype are presented in Section V. Finally, conclusions are drawn in Section VI.

## II. MODELING OF PPG SIGNALS

### A. Modeling of PPG Signal Corrupted by Artifacts

When motion artifacts and ambient light are introduced, the PPG signal can be expressed as

$$PPG = AC + DC + MA + AMB, \quad (1)$$

where AC and DC are the artifact-free AC and DC components, MA is the motion artifact, and AMB is the ambient light component. The AC component in PPG is generated by the changes in the blood volume near the measurement site, caused by the pulsation of the heart. The DC component, on the other hand, is formed by the reflection and scattering of light from the static tissue and the average blood volume [5]. The MA component is the fluctuation in PPG caused by changes in the incident angle and light path due to the sensor's movement relative to the skin, as well as internal deformations and structural changes in certain tissues [13]. Finally, the AMB component is caused by ambient light sources, which can be eliminated by CDS [19].

### B. PPG Signals Measured With Different Light Wavelengths

The AC/DC ratio of a PPG signal varies depending on the wavelength of light used for measurement [20], [21], [22]. When red and green LEDs are used for PPG measurement and the AMB components are canceled by CDS, the PPG signals can be expressed as

$$PPG_R = AC_R + DC_R + MA_R \quad (2)$$

$$\begin{aligned} PPG_G &= AC_G + DC_G + MA_G \\ &= \alpha \cdot AC_R + \beta \cdot DC_R + \gamma \cdot MA_R, \end{aligned} \quad (3)$$

where the subscripts *R* and *G* denote the red and green colors and  $\alpha$ ,  $\beta$ , and  $\gamma$  represent  $AC_G/AC_R$ ,  $DC_G/DC_R$ , and  $MA_G/MA_R$ , respectively. When the PPG signals are measured using closely placed LEDs, their MA components have a high correlation. Given that the formation of the motion artifact is

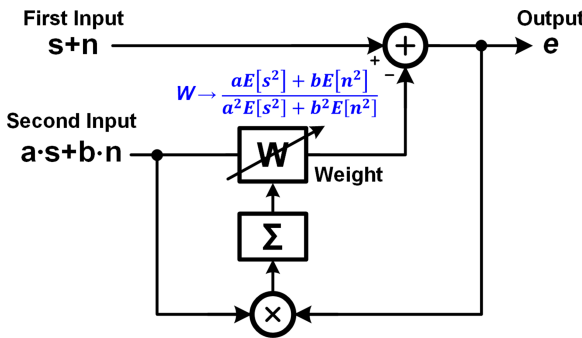


Fig. 2. Adaptive filter using LMS algorithm which receives the noise-added signal at both of its inputs.

largely attributed to the changes in the DC components,  $\beta \approx \gamma$ . Therefore,  $PPG_G$  can be modeled as

$$PPG_G \approx \alpha \cdot AC_R + \beta \cdot (DC_R + MA_R). \quad (4)$$

### III. MOTION ARTIFACT CANCELLATION

This section presents the proposed adaptive filter based motion artifact cancellation technique using the least mean squares (LMS) algorithm. We examine how the output of the adaptive filter converges when the inputs are the red and green PPG signals that contain both AC components and motion artifacts. In addition, the behavior of the adaptive filter will be examined when  $\beta$  is not a constant.

#### A. LMS Filter With Noise-Added Signals in Both Inputs

Adaptive filters can be used for real-time noise cancellation in time-varying environments [23]. They typically receive a noise-added signal and the noise as the inputs. When an LMS algorithm is used, the filter coefficients are updated so as to minimize the mean squared error at the output. As a result, the noise is canceled after it has settled.

Consider the LMS filter shown in Fig. 2, where the adaptive filter receives the noise-added signals at both of its inputs. In such a case, the noise is not completely canceled and remains at the output [24]. In detail, the output and its power can be expressed as

$$e = (1 - aW) \cdot s + (1 - bW) \cdot n \quad (5)$$

$$E[e^2] \approx E[(1 - aW)^2 \cdot s^2] + E[(1 - bW)^2 \cdot n^2], \quad (6)$$

where  $a$  and  $b$  are nonzero constants,  $s$  and  $n$  are the signal and noise components in the inputs, respectively, and  $W$  is the filter coefficient (i.e. the weight). Note that the  $E[s \cdot n]$  term is neglected in (6) since it is assumed that  $s$  and  $n$  are independent. The derivative of the output power is

$$\nabla_W E[e^2] = 2a \cdot (aW - 1) \cdot E[s^2] + 2b \cdot (bW - 1) \cdot E[n^2], \quad (7)$$

and since the LMS algorithm minimizes the output power,  $W$  converges to

$$W \rightarrow \frac{a \cdot E[s^2] + b \cdot E[n^2]}{a^2 \cdot E[s^2] + b^2 \cdot E[n^2]}. \quad (8)$$

Consequently, from (5) and (8), the output  $e$  converges to

$$e \rightarrow \frac{b(b-a) \cdot E[n^2]}{a^2E[s^2] + b^2E[n^2]} \cdot s + \frac{a(a-b) \cdot E[s^2]}{a^2E[s^2] + b^2E[n^2]} \cdot n. \quad (9)$$

While the noise component is not canceled at the output, it can be significantly reduced if  $E[n^2] \gg E[s^2]$  and  $a \neq b$ , in which case the weight converges to  $1/b$ .

#### B. LMS Filter With Red and Green PPG Signals as Inputs

When the red and green PPG models from (2) and (4) are applied to the input of the adaptive filter described earlier,  $AC_R$  becomes  $s$ , while  $DC_R + MA_R$  becomes  $n$ .

Since  $E[(DC_R + MA_R)^2] \gg E[AC_R^2]$  and  $\alpha \neq \beta$ , the weight converges to

$$W \rightarrow \frac{\alpha \cdot E[AC_R^2] + \beta \cdot E[(DC_R + MA_R)^2]}{\alpha^2 \cdot E[AC_R^2] + \beta^2 \cdot E[(DC_R + MA_R)^2]} \approx \frac{1}{\beta}, \quad (10)$$

and the output converges to

$$e \rightarrow (1 - \frac{\alpha}{\beta}) \cdot AC_R. \quad (11)$$

Therefore, the adaptive filter eliminates the DC and MA. Note that even in the absence of motion artifacts, the output converges to the same value since  $E[DC_R^2] \gg E[AC_R^2]$ . In addition, to acquire a large  $AC_R$  at the output,  $|1 - \alpha/\beta|$  should be maximized. Since  $\alpha$  and  $\beta$  are determined by the wavelengths of the LED light, it is important to select the wavelengths which have a large  $\alpha/\beta$ . By the definition of the  $\alpha$  and  $\beta$ , the  $\alpha/\beta$  can be expressed as

$$\frac{\alpha}{\beta} = \frac{AC_G/AC_R}{DC_G/DC_R} = \frac{(AC/DC)_G}{(AC/DC)_R}. \quad (12)$$

Since the red PPG has a low AC/DC ratio and the green PPG has a high AC/DC ratio [21], using the red PPG as the first input and the green PPG as the second input results in a large AC component at the output due to the larger  $|1 - \alpha/\beta|$ .

To verify the proposed MA cancellation technique, a simulation is carried out and the results are presented in Fig. 3. In the simulation, the red and green PPG signals are modeled as sinusoids with a frequency of 96 bpm. The AC/DC ratio of the red PPG is set to 1 %, and the  $\alpha$  and  $\beta$  are set to 0.3 and 0.7, respectively, for the case where the gain is small. The motion artifacts are modeled by a band-limited white Gaussian noise filtered by a sinc<sup>3</sup> filter with a 3-dB bandwidth of 2.29 Hz. The resulting waveforms of the red and green PPG signals with and without motion artifacts are shown in Fig. 3(a). When the LMS filter starts its operation, the weight  $W$  starts to converge to  $1/\beta$  regardless of the presence of motion artifacts as shown in Fig. 3(b). The output accordingly converges to  $(1 - \alpha/\beta) \cdot AC_R$ , as shown in Fig. 3(c). Finally, the error between the outputs converges to zero as shown in Fig. 3(d), which proves that the large DC and MA components of the PPG are canceled through the LMS algorithm.

#### C. Convergence and Settling of LMS Filter

Although it is assumed that the adaptive filter converges in the previous section, it can diverge if the learning rate is not

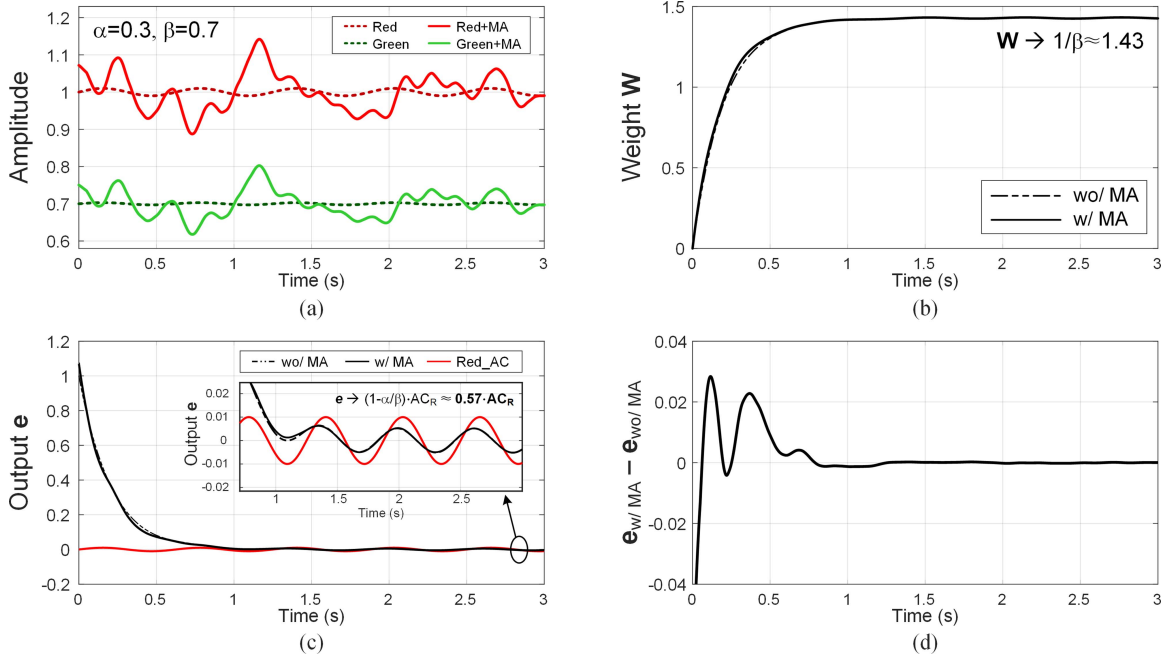


Fig. 3. Simulation results of the proposed MA cancellation technique. PPG signals are modeled as sinusoids and the motion artifacts are modeled as a band-limited white Gaussian noise. (a) Modeled red and green PPG with and without motion artifact, (b) transient of the weight, (c) transient of the output, and (d) difference in output with and without motion artifacts.

set appropriately. In order to find the condition for convergence, let's look at the weight update equation of the adaptive filter shown in Fig. 2, which is given as

$$w[k] = w[k-1] + \mu \beta n \cdot (n - \beta n \cdot w[k-1]), \quad (13)$$

where  $w[k]$  denotes the  $k$ -th sample of the weight sequence,  $\mu$  is the learning rate, and  $b = \beta$ . Note that  $s$  is disregarded here as it is much smaller than  $n$ . Therefore, the weight can be expressed as

$$w[k] = (1 - \mu \beta^2 n^2)^{k-1} \cdot \left( w[0] - \frac{1}{\beta} \right) + \frac{1}{\beta}, \quad (14)$$

where  $w[0]$  is the initial value. The convergence condition of the LMS filter is  $|1 - \mu \beta^2 n^2| < 1$ , and accordingly, the learning rate must be set in the range of  $0 < \mu < 2/\beta^2 n^2$ . Note that we can also verify that  $W$  converges to  $1/\beta$  as  $k \rightarrow \infty$ . In addition, since (14) is an exponentially decaying discrete time sequence, its time constant  $\tau$  can be calculated as

$$\tau = -\frac{T_s}{\ln |1 - \mu \beta^2 n^2|} \approx \frac{T_s}{\mu \beta^2 n^2}, \quad (15)$$

where  $T_s$  is the time interval between the weight updates, which is typically the same as the sampling rate of the PPG signals [25]. Note that the approximation is valid when  $0 < \mu \ll 1/\beta^2 n^2$ . This equation indicates that faster convergence can be achieved by increasing the learning rate. However, a large  $\mu$  causes large fluctuations in the weight, which can degrade the performance of the MA cancellation [25].

In a practical situation,  $\beta$  can change with the user's motion. If the change is too quick,  $W$  cannot settle to the desired value and thus the MA will not be effectively canceled. To see how

fast of a  $\beta$  that the adaptive filter can handle,  $W$  is monitored as  $\beta$  changes its frequency. If the speed of the adaptive filter is fast enough, then  $W$  will settle to  $1/\beta$ . Otherwise,  $W$  will settle to a different value. A simulation is carried out where  $\mu = 0.0005$ ,  $T_s = 10 \mu s$ ,  $\beta = 0.7 + 0.1 \sin(2\pi ft)$ ,  $n = 1$ , together with the band-limited random motion artifact. The result is shown in Fig. 4, where it can be seen that  $W$  follows  $1/\beta$  with a small error when  $\beta$  changes slowly, but the error becomes larger as the frequency of  $\beta$  increases.

It should be noted that while  $\beta$  can be affected by motion, it does not change at the same rate as the motion. Since  $\beta$  is the ratio of  $DC_G$  to  $DC_R$ , even if the motion causes a change in the DC value, it has nearly the same effect on  $DC_G$  and  $DC_R$ , and thus the ratio between the two values does not change significantly. Consequently, the change in  $\beta$  is not only relatively smaller compared to the MA, but the rate of change is also slower. This is empirically verified through measurements in Section V.

#### IV. IMPLEMENTATION

A prototype has been implemented to verify the proposed technique, and the architecture is shown in Fig. 5. The prototype is divided largely into two parts, the analog front end (AFE) including LED drivers, transimpedance amplifier (TIA), and ADC, and the digital back end (DBE) including demultiplexer (DEMUX), CDS, LMS, and LPF.

##### A. Analog Front-End

There are two LED drivers for the red and green LEDs whose intensity is controlled by resistors. As shown in Fig. 5, the LED on-time is managed by  $CLK_{red}$  and  $CLK_{green}$ . Both clocks

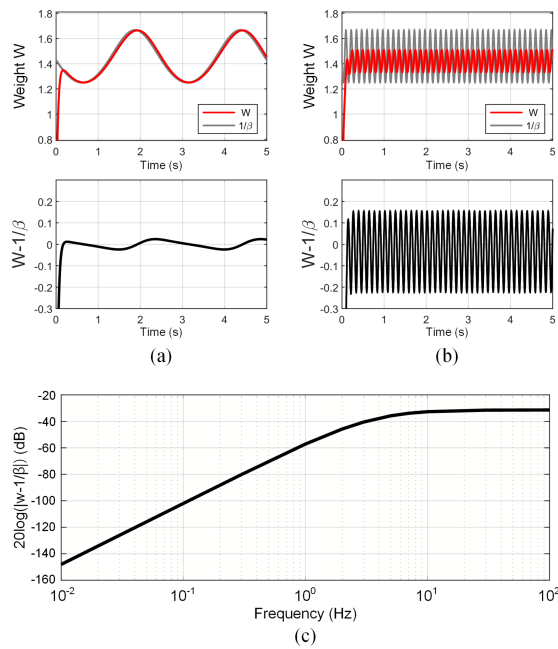


Fig. 4. Settling of the weight  $W$  when  $\beta$  is changing at the frequency of (a) 0.5 Hz and (b) 8 Hz, and (c) the magnitude of settling error.

possess a frequency of 100 Hz and a 30% duty cycle. For the remaining 40% of the period, both LEDs are turned off. The LED clock is generated from Arduino Nano 33 BLE [26]. In the PD, a time-division multiplexed (TDM) photocurrent is produced, consisting of red PPG, green PPG, and ambient light.

The schematic of the TIA is shown in Fig. 6. The input current  $I_{IN}$  is amplified by the TIA with a gain of  $1 \text{ M } \Omega$ . Since the TIA output needs to settle within the 30 % duty cycle of the 100 Hz LED clocks, its bandwidth is set to 1.94 kHz. An operational amplifier OPA2350 [27] is used in TIA. An anti-aliasing filter (AAF) is connected in series before the ADC to prevent aliasing, and its bandwidth is set to 1.6 kHz. An embedded 12-bit ADC in the Arduino Nano 33 BLE [26] is used for analog-to-digital conversion. The ADC has a sampling rate of 64 kHz, and its output undergoes decimation by a factor of 32 to obtain additional 2.5-bit resolution [28]. Since the input full range is  $3.3\mu \text{A}$ , the input current resolution of our AFE is 0.14 nA. When the AC component of the input PPG signal is greater than  $2 \text{ nA}_{pp}$ , the SNR of the AC component becomes greater than 25 dB, and thus the HR can be measured within  $\pm 1 \text{ bpm}$  error [19]. Note that our prototype is aimed at accurate HR estimation and is not intended for SpO<sub>2</sub> measurement, in which case the resolution may not be enough.

### B. Digital Back-End

The output of the ADC is first demultiplexed into red PPG, green PPG, and ambient light by sampling the decimated ADC output at the end of each period. The block diagram of the CDS and the adaptive filter based on the LMS algorithm is shown in Fig. 7. In CDS, the sampled ambient light component is subtracted from the red and green PPG signals. The offset and  $1/f$  noise from the AFE are also suppressed [29]. Next, the red

and green outputs of the CDS are fed to the adaptive filter to cancel the motion artifact. Note that the sign-sign LMS (SS-LMS) algorithm is adopted since it greatly reduces the requirement of the computational resource [30], which facilitates the on-chip implementation. The output of the adaptive filter is low-pass filtered with a cutoff frequency of 5 Hz to remove the remaining out-band noise, such as 60 Hz main noise aliased to 40 Hz.

To accurately estimate the power and area of the proposed scheme, it is designed using a 0.18  $\mu\text{m}$  CMOS process. The inputs are set as 12-bit binary values, and the output and internal nodes, including the filter coefficient, are configured as Q12.20 fixed-point values. The update rate is 100 Hz, which is the same as the sampling rate, and the learning rate is 0.005. Its size is 0.254 mm<sup>2</sup> and its power consumption is 30 nW.

## V. MEASUREMENT RESULTS

To verify the proposed motion artifact cancellation technique, PPG signals are measured under various activities. The experiment setup is shown in Fig. 8, where the chest ECG and finger PPG are measured simultaneously for 30 seconds. Chest ECG is measured using a commercial device MAX30003 [31]. Since ECG is robust against motion artifacts, it is used as a ground truth for heart rate [10]. For PPG measurement, a prototype of the front-end is implemented using commercial devices (SM1206 [32], [33], red and green LEDs, PDB-C171SM [34], PIN photodiode). The LEDs are placed 2 mm apart to minimize the size of the overall HR sensor, and it also ensures a high correlation in motion artifacts. The red and green LEDs consume 1.28 mA and 0.64 mA, respectively, from a 3.3 V supply, while the TIA and ADC consume 7.92 mA from a 5 V supply. The size of the PCB is 3.0 mm  $\times$  3.3 mm.

### A. Ambient Light Cancellation

The measured ambient light, red, and green PPG signals are shown in Fig. 9. The black lines represent the inputs of the CDS, while the colored lines represent the outputs of the CDS. During the measurement process, a light source is directed near the measurement site to observe the effect of ambient light. After applying CDS, the ambient light components are effectively removed, and the PPG signals are recovered. Note that the AC components of the red and green PPG signals are  $70 \text{ mV}_{pp}$  and  $46.7 \text{ mV}_{pp}$ , corresponding to  $70 \text{ nA}_{pp}$  and  $46.7 \text{ nA}_{pp}$  of the input current. Since both are greater than  $2 \text{ nA}_{pp}$ , the HR can be measured within  $\pm 1 \text{ bpm}$  of error as discussed in Section IV-A.

### B. Motion Artifact Cancellation

After CDS, the remaining motion artifact is canceled using the adaptive filter. The filter coefficient  $W$ , internal nodes, and output are presented in Fig. 10. When the adaptive filter begins to operate while the subject is in the stationary state,  $W$  converges to  $1/\beta$ . After  $W$  settles, we can see that  $W \cdot PPG_R$  follows  $PPG_R$ . Since the DC component is canceled by the adaptive filter, the pulsatile AC component is shown at the output. When the subject starts to squat, a large motion artifact is introduced in  $PPG_R$ . However, the motion artifact is canceled at the output

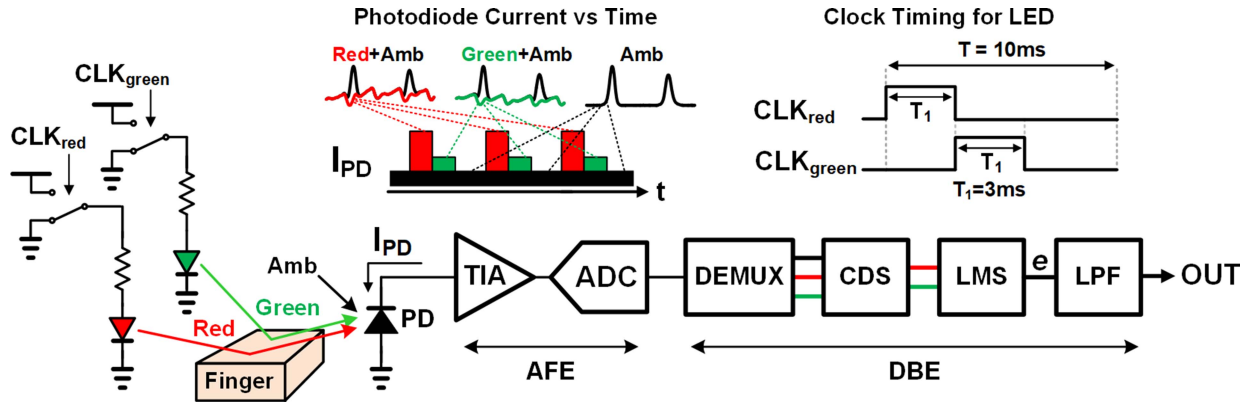


Fig. 5. System architecture of the prototype for verification of the proposed motion artifact cancellation technique.

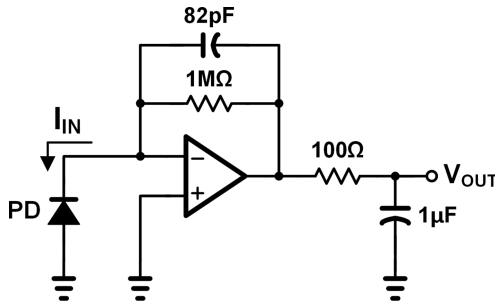


Fig. 6. Schematic of TIA and AAF.

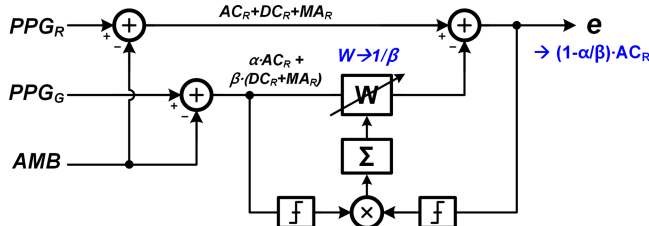


Fig. 7. Block diagram of the CDS and adaptive filter using SS-LMS algorithm.

since  $W$  is continuously adjusted by the SS-LMS algorithm. Note that  $W$  has a small variation during squatting, which verifies our assumption in Section III-C that  $\beta$  doesn't change much.

To see the effectiveness of the proposed motion artifact cancellation technique, the frequency spectrum is also observed for the red PPG,  $W$ , and the output of the adaptive filter, as shown in Fig. 11. In the red PPG, large motion artifact components are observed. However, the motion artifact is effectively canceled in the output, showing a clear pulsatile waveform. In the output spectrum, the nearest frequency component of MA is reduced by 22.63 dB.

To verify whether the output retains HR information, its peak locations are compared with the R-peaks of the simultaneously measured chest ECG in Fig. 12. A bandpass filtered PPG signal, with a passband of 1-5 Hz, is also provided for a baseline comparison. For synchronization of the ECG and PPG signals, the cross-correlation and the mean squared error (MSE) between

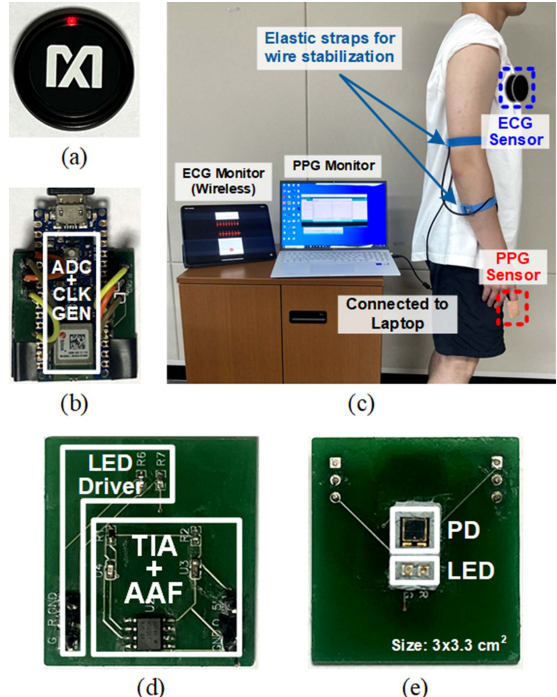


Fig. 8. Measurement setup for simultaneous monitoring of ECG and PPG. (a) MAX30003, (b) prototype of the AFE, (c) measurement setup, (d) front and (e) back sides of the PPG sensor module.

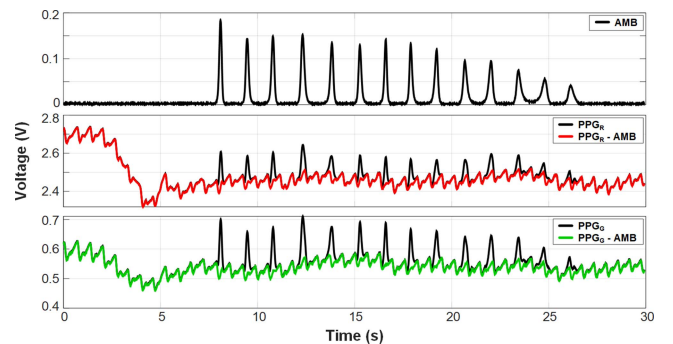


Fig. 9. Measured PPG signals with ambient light. The signals before CDS are drawn in black lines and the signals after CDS are drawn in colored lines. The ambient light source is a moving flashlight near the measurement site.

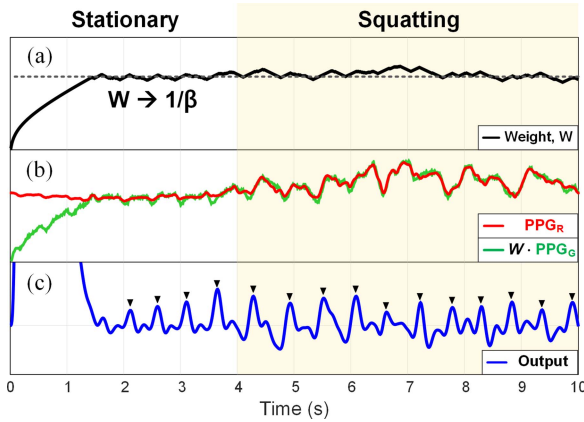


Fig. 10. Transients of the adaptive filter's internal parameters during squatting: (a) the weight updated by SS-LMS algorithm, (b) red and weighted green PPG, and (c) lowpass filtered adaptive filter output.

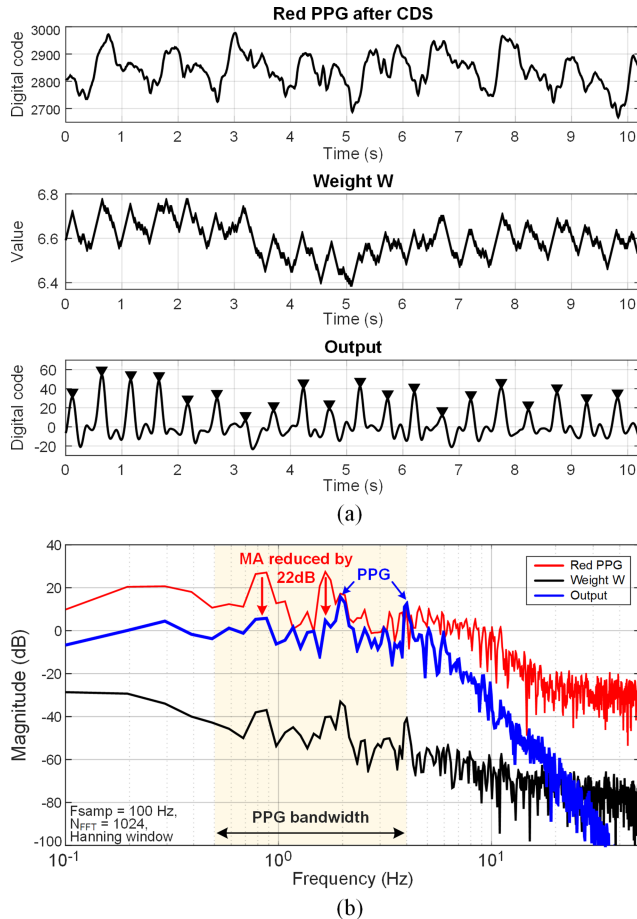


Fig. 11. Measured red PPG, weight, and output of the adaptive filter during walking. The output is filtered to remove the out-band noise. (a) Transient waveforms after settling of the SS-LMS filter and (b) their spectrum.

the peak positions in both ECG and PPG signals are calculated. The delay between the signals corresponds to the time interval which results in the highest correlation value and the lowest value of MSE. This delay is then used to adjust the signals, ensuring their synchronization. It can be seen that the peak locations of the adaptive filter output are closely aligned with

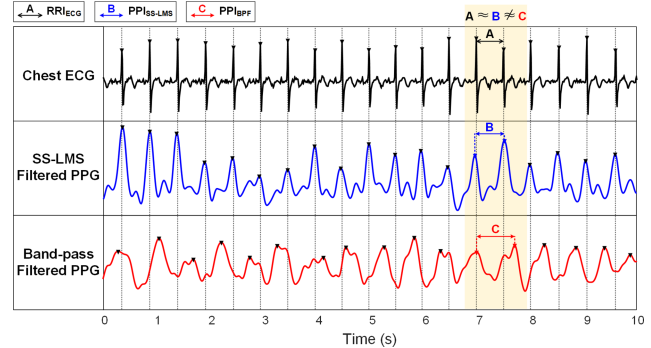


Fig. 12. Comparison of peak locations between simultaneously measured chest ECG, SS-LMS filtered PPG, and band-pass filtered PPG signals.

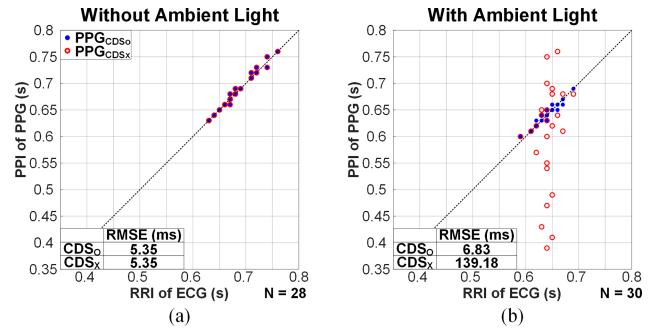


Fig. 13. Comparison of HBI accuracy between the presence and absence of CDS under two lighting conditions: (a) without ambient light and (b) with ambient light. N represents the number of data points collected during the 30-second measurement period.

the R-peaks of the chest ECG. However, the peak locations of the bandpass filtered PPG are not aligned with the R-peaks of ECG due to the motion artifact.

### C. Heart Rate Monitoring

To see the performance of the proposed techniques for HR monitoring, heart beat interval (HBI) from PPG signals is compared with the ECG signal. The peak intervals are represented on a scatter plot and a root mean squared error (RMSE) is calculated from the measured data for 30 seconds. The R-R intervals (RRI) of the ECG are used as the HR reference, and the peak-to-peak intervals (PPI) of the PPG signals are compared to the RRI.

To examine the influence of CDS on the proposed MA cancellation technique, ECG and PPG signals are measured with and without ambient light and the results are shown in Fig. 13. When there is no ambient light, it can be seen that the PPI of PPG is similar to the RRI of the ECG, regardless of the CDS technique. When ambient light is present, the PPI of PPG closely follows the RRI of the ECG only when the CDS is applied. The RMSE of HR is improved about 26 times with the CDS.

To demonstrate the proposed MA cancellation technique in a wearable environment, both ECG and PPG were measured during four different scenarios: stationary, squatting, walking, and running. The test scenarios except for the stationary case are shown in Fig. 14, with subjects instructed to swing their arms during the measurement. Although the speed of walking and

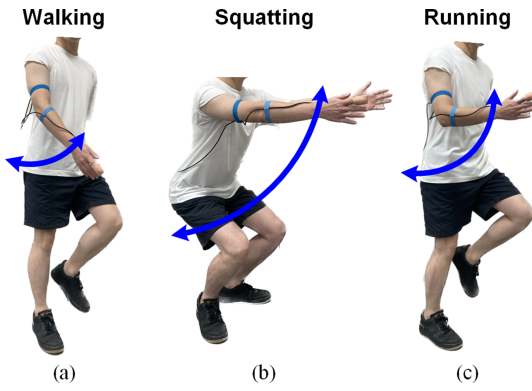


Fig. 14. Tested motion scenarios: (a) walking, (b) squatting, and (c) running.

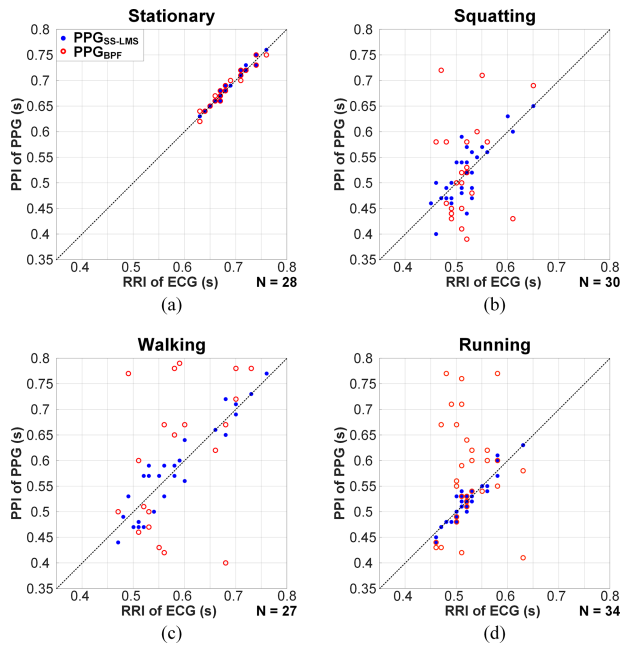


Fig. 15. Comparison of HBI accuracy between the proposed SS-LMS filtering and bandpass filtering across four motion scenarios: (a) stationary, (b) squatting, (c) walking, and (d) running. N represents the number of data points collected during the 30-second measurement.

running was not strictly controlled, the frequency components of the motion artifact fell within the PPG bandwidth (0.5-5 Hz). The measured PPI-RRI pairs for all motion scenarios are plotted on the scatter plots in Fig. 15. As can be seen, the HBI from the PPG and ECG are in close agreement when the subject is stationary. However, in the other three motion scenarios, the bandpass filtered PPG introduces a significant error in the HBI, while the MA-canceled PPG shows improved accuracy.

To evaluate the performance of the proposed technique, three error indicators for HR are calculated: cross-correlation coefficient ( $r$ ), coefficient of determination ( $R^2$ ), and RMSE. The results are shown in Fig. 16. It can be seen that the proposed technique yields considerably better values compared to using the BPF. The  $r$  and  $R^2$  with the proposed technique are much closer to 1 than those of the BPF, and the RMSE is reduced by 86.49 %, 87.54 %, and 89.09 % for squatting, walking, and

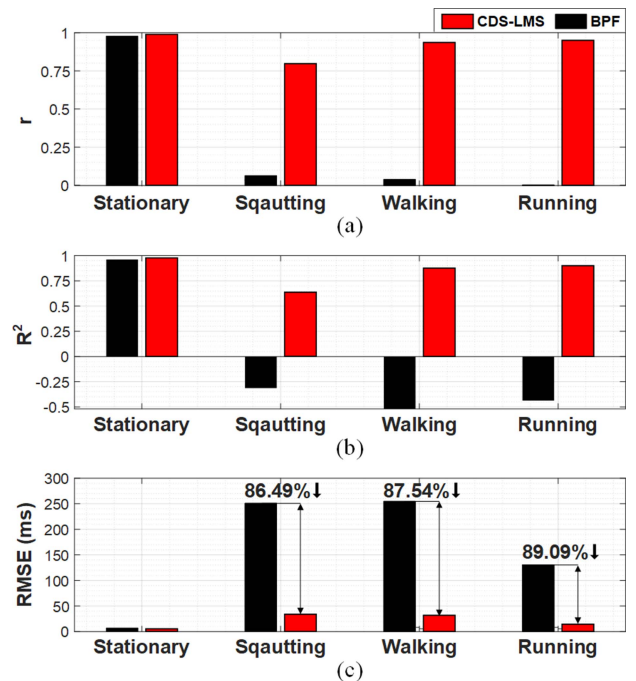


Fig. 16. Comparison of error indicators in measured HR during four motion scenarios processed by the proposed technique and conventional bandpass filtering. (a)  $r$ , (b)  $R^2$ , and (c) RMSE.

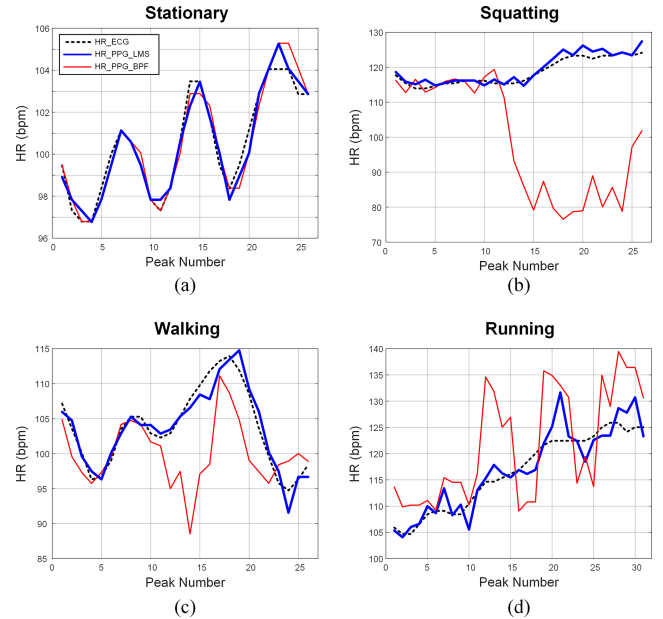


Fig. 17. The estimated HR from chest ECG, PPG with the proposed technique, and band-pass filtered PPG across four motion scenarios: (a) stationary, (b) squatting, (c) walking, and (d) running.

running, respectively. In addition, the estimated HR from the PPG signals with the proposed technique is compared with the HR from the chest ECG and band-pass filtered PPG. The HR is calculated from the HBI after moving average with a length of 3, and the result is shown in Fig. 17. It can be seen that the error is smaller in all the motion scenarios with the proposed technique.

TABLE I  
MEAN ABSOLUTE ERROR (MAE) IN ESTIMATED HR (IN BPM)

| Subjects | Stationary |      | Squatting |       | Walking |       | Running |       |
|----------|------------|------|-----------|-------|---------|-------|---------|-------|
|          | LMS        | BPF  | LMS       | BPF   | LMS     | BPF   | LMS     | BPF   |
| 1        | 0.32       | 0.43 | 2.06      | 17.87 | 1.25    | 8.96  | 1.80    | 5.41  |
| 2        | 0.36       | 0.44 | 1.07      | 20.36 | 1.22    | 4.87  | 2.02    | 8.11  |
| 3        | 0.31       | 0.35 | 1.05      | 12.74 | 0.80    | 7.20  | 1.01    | 8.36  |
| 4        | 0.26       | 0.50 | 1.65      | 7.48  | 1.01    | 18.89 | 1.39    | 6.79  |
| 5        | 0.33       | 0.77 | 1.78      | 5.82  | 1.18    | 5.67  | 2.16    | 8.12  |
| 6        | 0.19       | 0.35 | 1.28      | 5.59  | 1.19    | 12.57 | 2.69    | 12.11 |
| Mean     | 0.30       | 0.48 | 1.48      | 11.64 | 1.11    | 9.69  | 1.84    | 8.15  |

TABLE II  
COMPARISON WITH MOTION ARTIFACT CANCELLATION TECHNIQUES USING  
MULTI-WAVELENGTH PPG FOR HR ESTIMATION

|                           | [16]  | [13]                              | [17]                                    | This work                       |
|---------------------------|---|-----------------------------------|---|---------------------------------|
| Method                    | NLMS  | SVD, CWT, SSA                     | ICA, SVD                                | SS-LMS                          |
| Measurement Site          | Finger  | Wrist                             | Wrist                                   | Finger                          |
| # of PPG Channels         | 2   | 2                                 | 12                                      | 2                               |
| Window Size (s)           | 6   | 8                                 | 5                                       | 2-3 <sup>f</sup>                |
| Light Wavelengths of LEDs | Red (660n)<br>IR (895n)                         | Green (530n)<br>IR (940n)         | Red (655n)<br>Green (530n)<br>IR (940n) | Red (630n)<br>Green (523n)      |
| Motion Scenarios          | Hand Motions <sup>a</sup><br>Walking<br>Running | Arm and hand motions <sup>c</sup> | Walking<br>Running                      | Walking<br>Running<br>Squatting |
| # of Subjects             | 6   | 6                                 | 8                                       | 6                               |
| MAE <sub>HR</sub> (bpm)   | 2.7 <sup>b</sup>                                | 0.6 / 0.9 / 2.1 <sup>d</sup>      | -                                       | 1.1 / 1.8 / 1.5 <sup>h</sup>    |
| FDR (%) <sup>g</sup>      | -   | -                                 | 0.45 / 0.77 / 0.17 <sup>e</sup>         | -                               |

<sup>a</sup> Up-down/left-right motions of the hand and bending fingers. <sup>b</sup> Averaged for all motions  
<sup>c</sup> Finger tapping, waving/shaking, running arm swing, fist opening/closing, radial/ulnar deviation, and wrist extension/flexion <sup>d</sup> For periodic/random/continuous, non-periodic hand motions  
<sup>e</sup> For walking/fast-walking/running <sup>f</sup> Moving average in HR with the window length  $L = 3$   
<sup>g</sup> Failed Detection Rate = (True Positive)/(False Positive)\*100 <sup>h</sup> For walking/running/squatting

For further validation of the proposed MA cancellation technique, the experiment was conducted on six subjects. In each experiment, HR was obtained by using the proposed technique with two PPGs and by using bandpass filtering on a green PPG. The mean absolute errors (MAE) were then calculated to compare the accuracy and the results are shown in Table I. It can be seen that the MAE of the proposed technique is significantly better than the bandpass filtering method for all subjects and scenarios; the average MAE is reduced from to 1.48 bpm with the proposed approach – a substantial reduction of 85.0 % compared to the bandpass filtering.

In Table II, the proposed MA cancellation method is compared with previous techniques using multi-wavelength PPG for HR estimation [13], [16], [17]. The proposed method achieves a comparable mean absolute error (MAE) in the estimated HR without using complex signal processing techniques such as ICA, SVD, and CWT [13], [17], and has a lower error compared to [16] with much simpler adaptive algorithm and half the window size. For a comparison with [13] and [17], we applied the proposed technique on the wrist PPG. Note that wrist PPG typically has a smaller AC component than finger PPG, and thus a readout with a wider dynamic range (DR) is required. As our prototype was designed for finger PPG, it had to be worn tightly on the wrist to obtain a sufficient SNR. An experiment was conducted for subject 2 in stationary and walking conditions, and the results are shown in Fig. 18. The

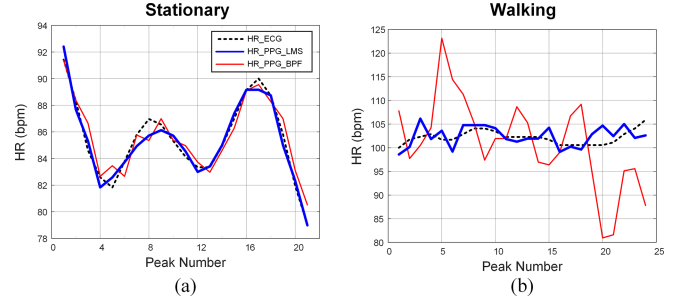


Fig. 18. Wrist PPG measurement results (a) in stationary and (b) during walking scenarios. The HR is estimated from chest ECG, the PPG processed with the proposed technique, and the bandpass filtered green PPG.

MAE of the proposed technique was 1.62 bpm, which is much smaller than the 7.61 bpm that was obtained using a bandpass filter on green PPG. This result validates our assumption that the red and green PPGs have different AC/DC ratios but the motion artifacts are highly correlated, even at the wrist.

## VI. CONCLUSION

In this article, an adaptive algorithm for motion artifact cancellation in PPG signals is proposed. The proposed technique exploits the high correlation in MA components and the different AC/DC ratios of two PPG signals measured by closely placed red and green LEDs. To mitigate the effects of random offset due to ambient light, CDS is applied prior to adaptive filtering. In an effort to minimize hardware resource usage, a sign-sign LMS algorithm is employed for the adaptive filter. To verify the proposed technique, a prototype was implemented and experiments were conducted with six subjects during three types of motion: walking, running, and squatting. As a result, the MAE in HR was reduced by an average of 85.0 %. This demonstrates that the proposed technique, despite using a much simpler algorithm, provides accuracy comparable to previous works.

## ACKNOWLEDGMENT

The authors would like to thank IC Design Education Center (IDEC) of Korea for their support.

## REFERENCES

- [1] K. Bayoumy et al., "Smart wearable devices in cardiovascular care: Where we are and how to move forward," *Nature Rev. Cardiol.*, vol. 18, no. 8, pp. 581–599, 2021.
- [2] D. Castaneda, A. Esparza, M. Ghamari, C. Soltanpur, and H. Nazeran, "A review on wearable photoplethysmography sensors and their potential future applications in health care," *Int. J. Biosensors Bioelectron.*, vol. 4, no. 4, 2018, Art. no. 195.
- [3] D. Ray, T. Collins, S. I. Woolley, and P. V. S. Ponnappalli, "A review of wearable multi-wavelength photoplethysmography," *IEEE Rev. Biomed. Eng.*, vol. 16, pp. 136–151, 2023.
- [4] D. Biswas, N. Simões-Capela, C. Van Hoof, and N. Van Helleputte, "Heart rate estimation from wrist-worn photoplethysmography: A review," *IEEE Sensors J.*, vol. 19, no. 16, pp. 6560–6570, Aug. 2019.
- [5] J. Allen, "Photoplethysmography and its application in clinical physiological measurement," *Physiol. Meas.*, vol. 28, no. 3, 2007, Art. no. R1.
- [6] Y. Sun and N. Thakor, "Photoplethysmography revisited: From contact to noncontact, from point to imaging," *IEEE Trans. Biomed. Eng.*, vol. 63, no. 3, pp. 463–477, Mar. 2016.

- [7] Q. Lin, W. Sijbers, C. Avidikou, C. Van Hoof, F. Tavernier, and N. Van Helleputte, "Photoplethysmography (PPG) sensor circuit design techniques," in *Proc. IEEE Custom Integr. Circuits Conf.*, 2022, pp. 01–08.
- [8] Z. Zhang, Z. Pi, and B. Liu, "TROIKA: A general framework for heart rate monitoring using wrist-type photoplethysmographic signals during intensive physical exercise," *IEEE Trans. Biomed. Eng.*, vol. 62, no. 2, pp. 522–531, Feb. 2015.
- [9] Z. Zhang, "Photoplethysmography-based heart rate monitoring in physical activities via joint sparse spectrum reconstruction," *IEEE Trans. Biomed. Eng.*, vol. 62, no. 8, pp. 1902–1910, Aug. 2015.
- [10] A. Temko, "Accurate heart rate monitoring during physical exercises using PPG," *IEEE Trans. Biomed. Eng.*, vol. 64, no. 9, pp. 2016–2024, Sep. 2017.
- [11] K. Arunkumar and M. Bhaskar, "Heart rate estimation from wrist-type photoplethysmography signals during physical exercise," *Biomed. Signal Process. Control*, vol. 57, 2020, Art. no. 101790.
- [12] H. Chung, H. Lee, and J. Lee, "Finite state machine framework for instantaneous heart rate validation using wearable photoplethysmography during intensive exercise," *IEEE J. Biomed. Health Inform.*, vol. 23, no. 4, pp. 1595–1606, Jul. 2019.
- [13] Y. Zhang et al., "Motion artifact reduction for wrist-worn photoplethysmograph sensors based on different wavelengths," *Sensors*, vol. 19, no. 3, 2019, Art. no. 673.
- [14] M. R. Ram, K. V. Madhav, E. H. Krishna, N. R. Komalla, and K. A. Reddy, "A novel approach for motion artifact reduction in PPG signals based on AS-LMS adaptive filter," *IEEE Trans. Instrum. Meas.*, vol. 61, no. 5, pp. 1445–1457, May 2012.
- [15] A. Kumar et al., "Reference signal less Fourier analysis based motion artifact removal algorithm for wearable photoplethysmography devices to estimate heart rate during physical exercises," *Comput. Biol. Med.*, vol. 141, 2022, Art. no. 105081.
- [16] R. Yousefi, M. Nourani, S. Ostadabbas, and I. Panahi, "A motion-tolerant adaptive algorithm for wearable photoplethysmographic biosensors," *IEEE J. Biomed. Health Inform.*, vol. 18, no. 2, pp. 670–681, Mar. 2014.
- [17] J. Lee, M. Kim, H.-K. Park, and I. Y. Kim, "Motion artifact reduction in wearable photoplethysmography based on multi-channel sensors with multiple wavelengths," *Sensors*, vol. 20, no. 5, 2020, Art. no. 1493.
- [18] W. Lee, P. Park, and S. Cho, "Reduction of motion artifact in PPG signal with CDS-LMS filter," in *Proc. IEEE Asia Pacific Conf. Circuit Syst.*, 2022, pp. 60–64.
- [19] A. Sharma et al., "A Sub-60- $\mu$ A multimodal smart biosensing SoC with -dB SNR, 35- $\mu$ A photoplethysmography signal chain," *IEEE J. Solid-State Circuits*, vol. 52, no. 4, pp. 1021–1033, Apr. 2017.
- [20] J. Lee, K. Matsumura, K.-i. Yamakoshi, P. Rolfe, S. Tanaka, and T. Yamakoshi, "Comparison between red, green and blue light reflection photoplethysmography for heart rate monitoring during motion," in *Proc. IEEE 35th Annu. Int. Conf. Eng. Med. Biol. Soc.*, 2013, pp. 1724–1727.
- [21] V. Vizbarra, "Comparison of green, blue and infrared light in wrist and forehead photoplethysmography," in *Biomed. Eng.*, vol. 17, no. 1, pp. 78–81, 2013.
- [22] Y. Maeda, M. Sekine, and T. Tamura, "The advantages of wearable green reflected photoplethysmography," *J. Med. Syst.*, vol. 35, pp. 829–834, 2011.
- [23] S. S. Chowdhury, R. Hyder, M. S. B. Hafiz, and M. A. Haque, "Real-time robust heart rate estimation from wrist-type PPG signals using multiple reference adaptive noise cancellation," *IEEE J. Biomed. Health Inform.*, vol. 22, no. 2, pp. 450–459, Mar. 2018.
- [24] B. Widrow et al., "Adaptive noise cancelling: Principles and applications," in *Proc. IEEE*, vol. 63, no. 12, pp. 1692–1716, Dec. 1975.
- [25] S. C. Douglas and M. Rupp, "Convergence issues in the LMS adaptive filter," in *The Digital Signal Processing Handbook*. Boca Raton, FL, USA: CRC, 2017, pp. 19–1.
- [26] Arduino, Arduino Nano 33 BLE, 2023, datasheet, Revision 2. Accessed: Jun. 4, 2023. [Online]. Available: <https://docs.arduino.cc/static/40270d2d33712208ed89f60010d0e187/ABX00030-datasheet.pdf>
- [27] Texas Instruments, OPAX350 High-Speed, Single-Supply, Rail-to-Rail Operational Amplifiers, 2015, datasheet, Revised Dec. 2015. Accessed: Jun. 4, 2023. [Online]. Available: <http://www.ti.com/lit/ds/symlink/opa350.pdf>
- [28] S. Pavan, R. Schreier, and G. C. Temes, *Understanding Delta-Sigma Data Converters*. Hoboken, NJ, USA: Wiley, 2017.
- [29] P. Schönen, F. Glaser, T. Burger, G. Rovere, L. Benini, and Q. Huang, "A multi-sensor and parallel processing SoC for miniaturized medical instrumentation," *IEEE J. Solid-State Circuits*, vol. 53, no. 7, pp. 2076–2087, Jul. 2018.
- [30] S. C. Douglas, "Introduction to adaptive filters," in *Digital Signal Processing Fundamentals*, V. K. Madisetti and D. B. Williams Boca Raton, FL, USA: CRC LLC, 1999.
- [31] Maxim Integrated, MAX30003: Ultra-Low Power, Single-Channel Integrated Biopotential (ECG, R to R Detection) AFE, 2021, datasheet, Revision 3. Accessed: Jun. 4, 2023. [Online]. Available: <https://datasheets.maximintegrated.com/en/ds/MAX30003.pdf>
- [32] BIVAR, SURFACE MOUNT LED HE RED, 1206 IL PACKAGE, 2014, datasheet, Revision A. Accessed: Jun. 4, 2023. [Online]. Available: [https://www.mouser.com/datasheet/2/50/SM1206NHC\\_IL-3002129.pdf](https://www.mouser.com/datasheet/2/50/SM1206NHC_IL-3002129.pdf)
- [33] BIVAR, SURFACE MOUNT LED PURE GREEN, 1206 IL PACKAGE, 2015, datasheet, Revision B. Accessed: Jun. 4, 2023. [Online]. Available: [https://www.mouser.com/datasheet/2/50/SM1206NPGC\\_IL-3002086.pdf](https://www.mouser.com/datasheet/2/50/SM1206NPGC_IL-3002086.pdf)
- [34] A. Photonix, PDB-C171SM, SMD Si Photodiode, 2016, datasheet, Revision A. Accessed: Jun. 4, 2023. [Online]. Available: [https://www.mouser.kr/datasheet/2/1418/DS\\_PDB\\_C171SM-2935440.pdf](https://www.mouser.kr/datasheet/2/1418/DS_PDB_C171SM-2935440.pdf)



**Pangi Park** (Graduate Student Member, IEEE) received the B.S. degree in biomedical engineering from Hanyang University, Seoul, South Korea, in 2019. He is currently working toward the Ph.D. degree in electrical engineering from the Korea Advanced Institute of Science and Technology, Daejeon, South Korea. His research interests include biomedical sensors, wearable healthcare system design, battery management ICs, reference circuits, and current sensor interfaces.



**Woobean Lee** (Student Member, IEEE) is currently working toward the bachelor's degree from the School of Electrical Engineering, Korea Advanced Institute of Science and Technology, Daejeon, South Korea. His research interests include low-power systems, wireless communication, and wearable biomedical sensor design.



**SeongHwan Cho** (Senior Member, IEEE) received the B.S. degree in electrical engineering from the Korea Advanced Institute of Science and Technology (KAIST), Daejeon, South Korea, in 1995, and the M.S. and Ph.D. degrees from Department of Electrical Engineering and Computer Science, Massachusetts Institute of Technology, Cambridge, MA, USA, in 1997 and 2002, respectively. In 2002, he joined Engim, Inc. Acton, MA, USA, where he was involved in data converters and phased-locked loop design for IEEE 802.11 abg WLANs. Since 2004, he has been with the School of Electrical Engineering, KAIST, where he is currently a Professor and the Department Head of semiconductor system engineering. He was with Marvell Inc., Santa Clara, CA, USA, from 2011 to 2012, and Google, London, U.K., from 2016 to 2017, as the Research Scientist. His research interests include analog and mixed-signal circuits for high-speed communication, low-power sensors, memory, and machine learning. Prof. Cho was the co-recipient of the 2009 IEEE Circuits and System Society Guillemin Cauer Best Paper Award and 2012 ISSCC Takuo Sugano Award for Outstanding Far-East Paper. He was the recipient of twice Outstanding Lecturer Award from KAIST. He has served on the Technical Program Committee on several IEEE conferences, including International Solid-State Circuits Conference, Symposium on VLSI and IEEE Asian Solid-State Circuits Conference. He was an Associate Editor for IEEE JOURNAL OF SOLIDSTATE CIRCUITS, IEEE TRANSACTIONS ON CIRCUITS AND SYSTEMS—I: REGULAR PAPERS, and a Distinguished Lecturer of the IEEE Solid-State Circuits Society.